



# Modeling the coupled aero-hydro-servo-dynamic response of 15 MW floating wind turbines with wind tunnel hardware in the loop

Alessandro Fontanella<sup>\*</sup>, Alan Facchinetti, Elio Daka, Marco Belloli

Mechanical Engineering Department, Politecnico di Milano, Milano, Via La Masa 1, 20156, Italy

## ARTICLE INFO

### Keywords:

Hardware in the loop  
Wind tunnel  
Floating wind turbine  
Wind turbine control

## ABSTRACT

Accurate modeling and design tools are required to lower the cost of floating wind and enable the rapid growth that is expected in the next years. This paper presents a hardware-in-the-loop (HIL) wind tunnel experiment, showing it is a valuable tool to investigate the coupled response of two 15 MW floating wind turbines. In the HIL experiment, the wind turbine is emulated with a physical scale model, that is a 1:100 version of the IEA 15 MW, with reference closed-loop control functionalities. Rotor aerodynamic loads are continuously measured and fed back to a numerical simulation of the floater response. The output of the simulation are platform motions that are recreated in the wind tunnel with a robot. The two floating wind turbines are tested with various wind, waves, and turbine control conditions. It is shown the turbine scaled model matches with good accuracy the response of the IEA 15 MW, thanks to the aerodynamic re-design of blades and the adopted closed-loop control strategy. The HIL control system reproduces the coupling between turbine and platform with very small errors. In operational conditions, aerodynamic damping of platform motion is sensitive to wind speed when the turbine is controlled in closed loop, and it is shown that this is due to the coupling between platform pitch and rotor. The amount of aerodynamic damping just below the rated wind speed is found to be more uncertain than in other wind conditions.

## 1. Introduction

Floating offshore wind turbines (FOWT) harness wind power in deeper waters than bottom-fixed turbines, opening offshore wind projects for sea basins such as the Mediterranean and Atlantic. The amount of energy produced with floating wind turbines is increasing rapidly: Europe has about 100 MW of FOWTs in operation, but has the ambition to install 10 GW of floating wind by 2030. This rapid growth is actually achievable only if the cost of floating wind turbine technology reduces to the same levels of bottom-fixed offshore wind. One key element to enable this cost reduction is the availability of accurate design tools. In this respect, scale model testing is more difficult than for conventional offshore structure due to the need to reproduce with equal accuracy phenomena that have very different physics, such as turbine structural response, wind and rotor aerodynamics, waves and platform hydrodynamics. Several scale model experiments have been carried out in the past where the turbine has been modeled with different methodologies [1], but there is still no general consensus on how to test FOWT scale models. At the same time, there are still many challenges ahead to understand how capable are offshore simulation codes to capture the additional complexity of floating wind

turbines, and experimental data is crucial to support their validation and development.

In this paper we report on the use of hardware-in-the-loop (HIL) to model the coupled aero-hydro-servo-dynamic response of 15 MW floating wind turbines in a wind tunnel experiment. The testing is conducted as part of the COREWIND project whose aim is to develop two concrete-based support platforms and anchoring systems to reduce the cost of floating wind. In COREWIND, wind tunnel experiments are carried out to understand the impact of aerodynamic loads and the action of the turbine controller on the floating turbine response.

Wind tunnel experiments have been used in recent past to study the aerodynamic response of floating wind turbines due to platform motion. These experiments have often made strong simplifying assumptions on the FOWT modeling to focus on a single aspect of the problem. In [2–4], the rotor aerodynamic loading is studied with prescribed platform motion along one degree-of-freedom. Motion is harmonic with low-frequency, to avoid exciting the flexible response of the turbine, and large amplitude, to have a large enough apparent wind. Moreover, in [2,3] rotor speed and blade pitch are fixed to constant values to isolate the effect of platform motion on rotor aerodynamics.

<sup>\*</sup> Corresponding author.

E-mail address: [alessandro.fontanella@polimi.it](mailto:alessandro.fontanella@polimi.it) (A. Fontanella).

When the focus of scaled testing was the global response of the floating structure, experiments were carried out in wave basin facilities, with physical modeling of the floating platform, mooring, waves, wind turbine, and wind. In [5] the 5 MW HyWind spar turbine was tested in a variety of environmental conditions and with several wind turbine control schemes. The experiment proved the coupling between platform motion and turbine controller and the possible instability problem deriving from it. The DeepCwind consortium conducted various experiments about the coupled response of three FOWT concepts, whose results are summarized in [6,7]. An important outcome of DeepCwind is that the aerodynamic response of geometrically-scaled rotors is not representative of full-scale turbines, due to the strong mismatch in Reynolds number [8]. The problem is circumvented by designing new blades that match the aerodynamic loads of the full-scale turbine despite the low Reynolds numbers that come with Froude scaling. The study of active turbine controls and their impact on floating wind turbine response was limited in the DeepCwind consortium. A further experiment about the DeepCwind semisubmersible was specifically carried out to assess the influence of active blade pitch and generator control on the FOWT global performance [9]. The influence of aerodynamic damping and interaction between wind, waves and blade pitch control on the response of a scale model version of the DTU 10 MW on top of the TripleSpar platform is investigated in the wave basin campaign of [10,11]. Three control strategies are compared showing the platform pitch mode becomes unstable when a standard land-based controller is applied. A scaled 10 MW tension-leg platform FOWT with active pitch control and various environmental conditions is tested in [12], revealing the onshore controller induces high oscillations in blade pitch and an increased response in surge. More recently, [13] carried out scale model experiments about a 15 MW floating wind turbine including active control, but, at the time of writing, only tests with fixed foundation have been published.

In parallel to wave basin experiments with a physical scale model of the entire FOWT, test methodologies based on HIL have been developed by various laboratories. In HIL testing, one portion of the FOWT, whose theoretical model is deemed uncertain, is reproduced with a physical scale model and the rest is emulated with a numerical model. The two subdomains are coupled by means of continuous measurement of some quantities of the physical model and actuation of other quantities computed in the numerical model.

Wave basin HIL assumes the turbine aerodynamics and control actions are described with good accuracy by a theoretical model (e.g., based on blade element momentum theory) hence emulating them numerically, whereas the hydrodynamic and structural response of the platform is deemed uncertain and is reproduced with a physical scale model. The HIL modeling of aerodynamic loads is compared to the use of a wind turbine scale model in [14] for a tension leg platform FOWT. In [15] the coupling between aerodynamic and hydrodynamic loads on a 12 MW semi-submersible FOWT is investigated in a HIL wave basin experiment, where aerodynamic loads are computed with a BEM model of the rotor based on measured platform motion and applied to the physical model of the platform and tower with a cable robot. It is shown that aerodynamic loads have an impact on the low-frequency surge and pitch response, but a minimal influence on the wave-frequency motion. In [16] a 10 MW FOWT is tested with HIL using a multi-fan system as a force actuator and it is shown that offshore codes do not capture variations in the platform pitch frequency due to variations in hydrostatic restoring platform that come with static tilt. The multi-fan HIL is utilized to carry out experiments with a scale model of the DeepCwind 5 MW and to study the influence of industry-standard control strategies on the FOWT global response in [17,18].

The code-to-code verification of [19] has shown that aerodynamic models are uncertain in some conditions, for example when platform motion is combined with active turbine control. HIL wind tunnel testing is the other side of the coin, because it assumes the aerodynamic loading is uncertain whereas waves, mooring and hydrodynamics can

**Table 1**  
Key parameters of the Activefloat substructure.

Parameter	Unit	Value
Column diameter	m	17
Column height	m	35.5
Column radius	m	34
Pontoon width	m	17
Pontoon height	m	11.5
Mass	t	$3.4 \times 10^7$
Vertical center of gravity (CG)	m	-113.08
$I_{xx}$ about CG	kg m <sup>2</sup>	$1.6 \times 10^{10}$
$I_{yy}$ about CG	kg m <sup>2</sup>	$1.6 \times 10^{10}$
$I_{zz}$ about CG	kg m <sup>2</sup>	$2.6 \times 10^{10}$

be well represented by theoretical models. Rotor aerodynamic loads of the scaled turbine are measured and fed back to a numerical simulation of the floater dynamics, hydrodynamics, and mooring. This simulation is run in real-time, in parallel to the physical part of the experiment, and its output is platform motion, which is created in the wind tunnel with a robot under the turbine. Wind tunnel HIL testing was used for the first time in [20] to study the impact of aerodynamic loads on platform surge and pitch motion of the DeepCwind 5 MW, with fixed rotor speed and blade pitch and various wind and wave conditions. The HIL setup of [20] only modeled surge and pitch dynamics; an improved 6-degrees-of-freedom HIL system is described in [21].

To the best of authors knowledge, there is no literature on the use of HIL to investigate the coupled aero-hydro-servo-dynamic of 15 MW floating wind turbines. The expected impact of addressing this scientific gap is to improve the modeling tools for utility-scale FOWTs and, at the same time, to advance knowledge about their global response. The main novel contributions of this article are:

1. to provide guidance on the use of HIL in conjunction with low-Reynolds rotor design and the use of closed-loop wind turbine control to model floating wind turbines in wind tunnel experiments;
2. to show the impact of wind turbine aerodynamics and controller action on the global response of 15 MW FOWTs with physical and accurate modeling of the turbine rotor.

The structure of this article is as follows. The two floating wind turbines of the experiment are briefly described in Section 2. The scaling, the experimental setup and the HIL methodology are presented in Section 3. The load cases are described in Section 4 and the results of the experiment are reported in Section 5. The article conclusions are drawn in Section 6. All values in the paper are given at full-scale unless otherwise noted.

## 2. Description of the floating wind turbines

The FOWTs object of the experimental testing are shown in Fig. 1. The Activefloat is a semi-submersible floater with three external columns connected to a central column by means of three pontoons. The platform draft is 26.5 m. The platform is anchored to the seabed with three symmetric catenary mooring lines made of chains that are attached to the three external columns. The main properties of the Activefloat modeled in the experiment are summarized in Table 1. The WindCrete is a spar floater with a draft of 155 m; the turbine tower and the spar form a single body made of concrete. The WindCrete has three catenary mooring lines with delta-shaped connections. The key parameters of the WindCrete platform modeled in the experiment are summarized in Table 2. The wind turbine of the two FOWTs is the IEA 15 MW [22]. In both cases, the hub height above mean sea level is 135 m. Additional details about the geometry and mass properties of the two floaters can be found in [23].

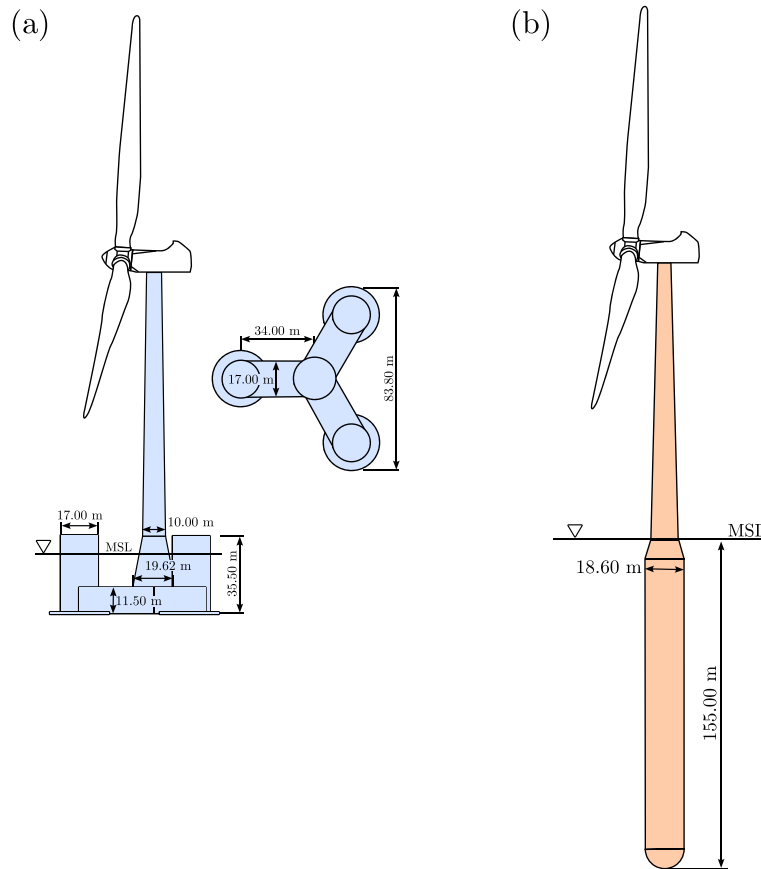


Fig. 1. The 15 MW floating wind turbines of the experimental campaign. (a) Activefloat. (b) WindCrete.

Table 2

Key parameters of the WindCrete substructure.

Parameter	Unit	Value
Spar diameter	m	18.60
Mass	t	$3.7 \times 10^7$
Vertical center of gravity (CG)	m	-17.529
$I_{xx}$ about CG	kg m <sup>2</sup>	$5.6 \times 10^{10}$
$I_{yy}$ about CG	kg m <sup>2</sup>	$5.6 \times 10^{10}$
$I_{zz}$ about CG	kg m <sup>2</sup>	$1.8 \times 10^9$

### 3. Description of the experimental setup

The experimental campaign was carried out in the atmospheric boundary layer test section of the Politecnico di Milano wind tunnel, which is 13.84 m wide  $\times$  3.84 m high  $\times$  35 m long. The two FOWTs are simulated with geometry scale factor  $\lambda_L = 1:100$ . At this scale the rotor diameter of the IEA 15 MW is 2.4 m. Differently from Froude scaling, which is the standard for wave basin experiments, in HIL wind tunnel testing the velocity scale factor is set independently of  $\lambda_L$ , and it is equal to  $\lambda_v = 1:3$ . The experimental setup is shown in Fig. 2 together with the coordinate systems (CS) used for the testing and data analysis.

The instrumentation includes an ATI Mini45 load cell with SI-580-20 calibration that measures the six-component force at the tower-nacelle interface. The free-stream wind speed is measured with a pitot tube at hub-height about 3 diameters upstream the wind turbine location. The nacelle acceleration in the direction of the CS2  $x$ -axis is measured with a MEMS accelerometer. Rotor speed is measured with the generator encoder. Measurement of the actual blade-pitch angle is not available and is replaced with the collective blade pitch set point. All measurements are acquired simultaneously with a NI DAQ with sampling frequency of 2000 Hz (corresponding to 60 Hz at full scale).

#### 3.1. Hardware-in-the-loop system

The experiment models the rigid-body motion of the FOWT with the equation:

$$\mathbf{M}_{\text{tot}} \ddot{\mathbf{q}}_s = \mathbf{F}_{\text{num}} + \mathbf{F}_{\text{wt},n} \quad (1)$$

where  $\mathbf{M}_{\text{tot}}$  is the platform inertia (mass and hydrodynamic added mass),  $\mathbf{q}_s$  is the vector of the platform rigid-body motions in CS1 (surge, sway, heave, roll, pitch, yaw) and it is the position set point to the robot;  $\mathbf{F}_{\text{num}}$  are hydrodynamic and mooring forces that are introduced in the experiment numerically;  $\mathbf{F}_{\text{wt},n}$  are the rotor aerodynamic loads on the platform that are reproduced with the wind turbine scale model and physical generation of wind inside the wind tunnel. Notice the rotor-nacelle inertia for rigid-body platform motions is simulated with the numerical model. The rotor inertia about the rotor axis is instead the inertia of the physical rotor.

The HIL system provides the link between the hydro-structural response of the platform and the servo-aerodynamic response of the rotor. Making things simple, it provides the “+” at the right hand side of Eq. (1). Fig. 3 shows the working principle of the HIL system. Tower-top loads measured with the load cell are continuously acquired by the HIL controller and projected in CS2 to get  $\mathbf{F}_{\text{wt}}$ . We preferred to have the load cell at tower-top rather than at tower base (like in [20,21]) because in this way the aerodynamic components are larger fractions of the signal, and to avoid introducing deformability at tower base that would reduce the frequency of the turbine first fore-aft mode. For increasing frequency,  $\mathbf{F}_{\text{wt}}$  is dominated by inertial loads of the rotor-nacelle assembly due to rigid-body motion of the platform and flexible response of the tower. To remove these contributions,  $\mathbf{F}_{\text{wt}}$  is filtered with the combination of a second-order Butterworth filter with cutoff frequency 3 Hz (corresponding to 0.09 Hz at full scale) and a second-order notch filter with frequency 9.5 Hz (0.285 Hz at full scale). The

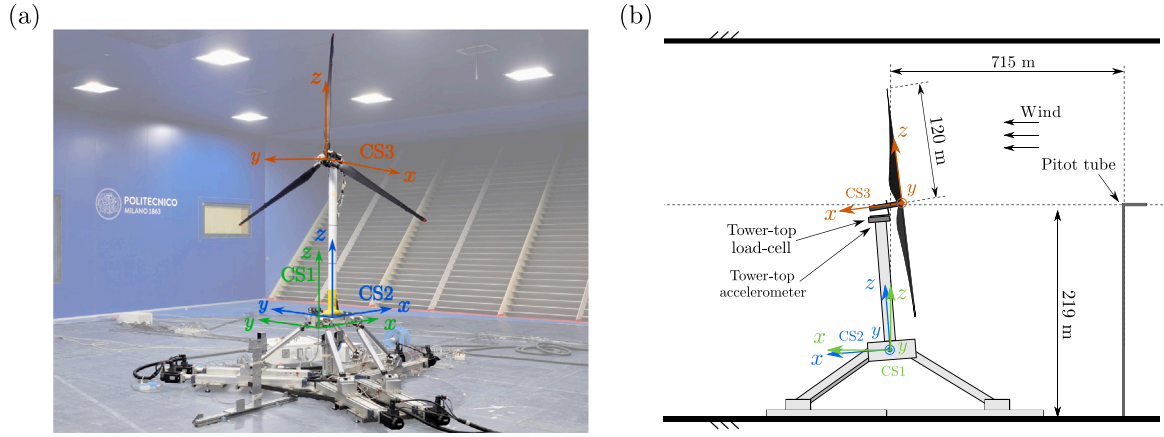


Fig. 2. Experimental setup. (a) The hardware-in-the-loop system inside the test section of Politecnico di Milano Wind Tunnel. (b) Main dimensions of the wind turbine scale model reported at full scale. CS are the coordinate systems: CS1 is earth-fixed, CS2 is fixed to the FOWT tower base and CS3 to the rotor hub.

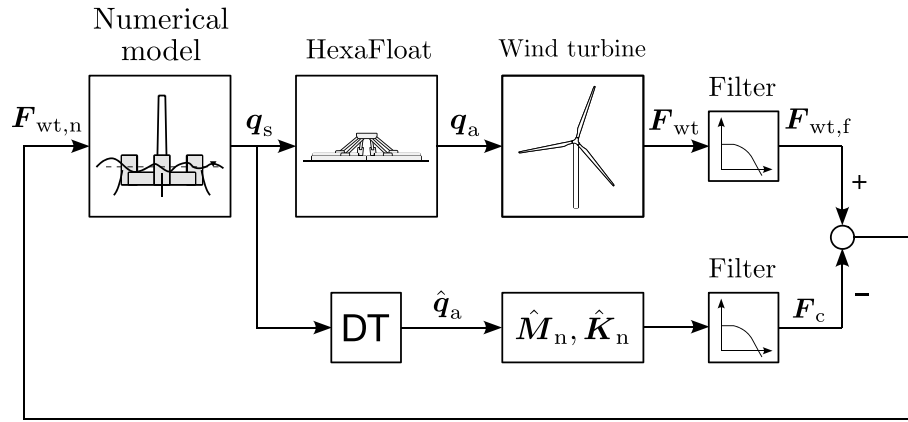


Fig. 3. Scheme of the hardware-in-the-loop system.

Butterworth filter is designed to have unity magnitude in the frequency range of platform rigid-body modes. Aerodynamic loads are expected to have a significant influence only at low frequency [15], thus the filter does not alter their signals at these frequencies. At higher frequencies, aerodynamic forces are small compared to wave and inertia forces, thus preserving the force feedback from the wind turbine is less important. The first fore-aft mode of the tower is placed about one frequency decade above the natural modes of the platform, in this way the notch filter does affect low-frequency force signals.

An estimate of rotor aerodynamic loads is obtained subtracting the inertia plus gravity loads  $F_c$  from the filtered force feedback:

$$F_{wt,n} = F_{wt,f} - F_c. \quad (2)$$

$F_c$  is the inertia and gravity loads of the rotor-nacelle assembly due to rigid-body motion of the structure. We call this operation force subtraction. With a linear formulation,  $F_c$  is calculated as:

$$F_c^* = \hat{M}_n \ddot{q}_a + \hat{K}_n \dot{q}_a, \quad (3)$$

where  $\hat{q}_a$  is the estimated actual platform motion. Mechanical loads are assumed proportional to the acceleration of the wind turbine with matrix  $\hat{M}_n$ , and to its position with matrix  $\hat{K}_n$ .  $\hat{M}_n$  and  $\hat{K}_n$  are obtained based on multi-body system dynamics theory. Following the procedure introduced in [24], the force  $F_c^*$  is filtered with the same filter applied to the wind turbine force to obtain  $F_c$  avoiding any undesired phase shift.

Platform motion computed from real-time integration of the floater numerical model is recreated in the physical subdomain of the experiment with a 6-DOFs robotic platform mounted at the bottom of

the turbine tower [25]. Calculation of the force-feedback with Eq. (3) requires the turbine actual position  $q_a$ . In our case, this is not available as a measurement, but it is estimated from the position set point  $q_s$  and a dynamic model of the robot ( $q_s \rightarrow \hat{q}_a$ ), which is assumed to behave as a time-delay system of time delay equal to 0.03 s (the problem of modeling the motion actuator of the HIL system is discussed in [24]).

### 3.2. Platform subdomain

The floating structure with mooring and waves forms the numerical subsystem, which is reproduced in the experiment by means of a simulation model. This model is based on Eq. (1), which is expanded to show the external forces of the platform subdomain, obtaining:

$$(\mathbf{M} + \mathbf{A}_\infty) \ddot{q}_s = \mathbf{F}_{hs} + \mathbf{F}_{moor} + \mathbf{F}_{rad} + \mathbf{F}_{ld} + \mathbf{F}_{wave} + \mathbf{F}_{visc} + \mathbf{F}_{wt,n}, \quad (4)$$

where  $\mathbf{M}$  is the mass matrix relative to the 6 rigid-body DOFs including contributions of the turbine and the platform,  $\mathbf{A}_\infty$  is the infinite-frequency added mass matrix of the floating platform  $\mathbf{F}_{hs}$  is the vector of hydrostatic loads,  $\mathbf{F}_{rad}$  of radiation forces,  $\mathbf{F}_{ld}$  of additional damping forces linearly proportional to platform velocity,  $\mathbf{F}_{wave}$  of first-plus second-order (difference frequency) wave-excitation loads from diffraction,  $\mathbf{F}_{visc}$  collects viscous drag forces,  $\mathbf{F}_{moor}$  the forces exerted by the mooring system on the platform DOFs.  $\mathbf{F}_{wt,n}$  is the vector of aerodynamics loading of the wind turbine rotor, obtained as explained in Section 3.1.

$\mathbf{F}_{hs}$ ,  $\mathbf{F}_{rad}$ ,  $\mathbf{F}_{wave}$ , are modeled numerically with potential flow theory, based on WAMIT data shared in the repository [26] for the

Activefloat and [27] for the WindCrete. Hydrostatic loads are:

$$F_{hs} = C_{hs}q_s, \quad (5)$$

where  $C_{hs}$  is the hydrostatic stiffness matrix. Radiation forces are approximated by means of a parametric model in state-space form that avoids the computational burden associated with the convolution integral of [28]:

$$\begin{cases} \dot{x}_r = \hat{A}_r x_r + \hat{B}_r \dot{q}_s \\ F_{rad} = \hat{C}_r x_r \end{cases}, \quad (6)$$

where  $x_r$  is the vector of states of the radiation model; matrices  $\hat{A}_r$ ,  $\hat{B}_r$ , and  $\hat{C}_r$  are obtained with the frequency-domain system identification method of [29], where the identification data are the frequency-dependent added mass and damping matrices of the WAMIT model. Wave loads are the sum of first- and second-order components  $F_{wave} = F_{wave}^1 + F_{wave}^{2,d}$ . First-order wave forces for the  $i$ th DOF are calculated as the discrete inverse Fourier transform of the wave excitation frequency response function  $X_{w,i}(\omega)$  of the WAMIT model multiplied by the complex wave spectrum  $\eta(\omega)$ :

$$F_{wave,i}^1(t) = \Re \sum_{n=1}^N X_{w,i}(\omega_n) \eta(\omega_n) e^{j\omega_n t}, \quad (7)$$

where  $N$  is the number of harmonic components,  $\eta(\omega)$  is the complex wave spectrum with random phase and magnitude defined from user-specified parameters. Second-order difference frequency wave loads are included in the experiment because these are an important source of excitation for FOWTs and their modeling is of critical importance [30]. Second-order wave loads for the  $i$ th DOF are computed as:

$$F_{wave,i}^{2,d}(t) = \Re \sum_{n=1}^N \sum_{m=1}^N \eta(\omega_n) \eta^*(\omega_m) D_{nm,i} e^{j(\omega_n - \omega_m)t}, \quad (8)$$

where  $D_{nm,i}$  is the complex difference-frequency second-order transfer function for the  $i$ th DOF part of the WAMIT model, and  $\eta^*$  is the complex conjugate of the wave spectrum. Viscous loads are obtained from a quadratic damping model:

$$F_{visc} = B_2 \dot{q}_s |\dot{q}_s|, \quad (9)$$

where  $B_2$  is the diagonal quadratic damping matrix. Additional damping forces are introduced as:

$$F_{ld} = B_1 \dot{q}_s, \quad (10)$$

where  $B_1$  is the linear damping matrix whose elements are tuned to match the damping ratio of platform modes. The damping ratio is identified in wave basin testing of the Activefloat and WindCrete carried out in the COREWIND project in parallel to the wind tunnel experiment [23]. Mooring forces are modeled with the linearized stiffness matrix of the mooring system in the FOWT rest position:

$$F_{moor} = K_c q_s. \quad (11)$$

Here, mooring forces follow a linearized representation because this requires less computational resources when simulated in real time and a study of nonlinear mooring loads is outside the scope of the present work. Linear approximations of mooring systems are used also in wave basin experiments, for example in [15,18]. In general, mooring loads are included in Eq. (4) as  $F_{moor} = f(\dot{q}_s, q_s)$ , where  $f(\cdot)$  is a nonlinear function. A numerical method to introduce nonlinear mooring dynamics in wind tunnel HIL experiments is presented in [31].

Eq. (4) is integrated in a time-marching simulation to compute the platform motion set point  $q_s$ . The numerical model is run at model scale to respect the time scale of the experiment.

**Table 3**

Key parameters of the IEA 15 MW (from [22]), of the wind turbine scale model reported at full-scale (WTM FS) and of the wind turbine scale model reported at model scale (WTM MS). ‘‘MSL’’ is mean sea level; WTM FS parameters are computed upscaling all WTM MS quantities by means of dimensional analysis with a length scale factor  $\lambda_L = 1 : 100$  and a velocity scale factor  $\lambda_v = 1 : 3$ .

Parameter	Unit	IEA 15 MW	WTM FS	WTM MS
Rotor diameter	m	240	240	2.4
Rated wind speed	m/s	10.59	10.59	3.53
Rated rotor speed	rpm	7.56	7.56	252
Rated TSR	–	9	9	9
Hub diameter	m	7.94	18.00	0.18
Hub overhang	m	11.35	13.90	0.14
Shaft tilt angle	°	6	5	5
Rotor precone angle	°	–4	0	0
Blade mass	kg	$65 \times 10^3$	$240 \times 10^3$	0.24
Rotor inertia	kg m <sup>2</sup>	$0.31 \times 10^9$	$2.79 \times 10^9$	0.279
Rotor nacelle assembly mass	kg	$1017 \times 10^3$	$4016 \times 10^3$	4.016

### 3.3. Wind turbine subdomain

The physical part of the experiment is the wind turbine scale model whose key parameters are reported in Table 3. Rotor blades are designed according to the methodology of [32] to replicate at TSR = 9 the normal force distribution of the IEA 15 MW blades despite a reduction in Reynolds of 1:300. FFA-W3 airfoils of the IEA 15 MW are replaced with the SD7032 due to suitable characteristics at  $Re \approx 300 \times 10^3$ . Chord and twist of the full-scale turbine are altered with respect to their geometrically-scaled value to match the distribution of steady lift force and its variation with angle of attack. The wind turbine scale model has the ability to apply active control to generator and individual-blade pitch, although in this case the blade pitch is controlled collectively.

The blade geometry and the experimentally-measured polars of the SD7032 are used to build a model of the rotor in OpenFAST (v3.3.0). Aerodynamic calculations are done in AeroDyn15 based on dynamic blade-element momentum theory. The OpenFAST model is utilized in this work for cross-validation of the rotor aerodynamic response versus experimental measurements, and to verify the closed-loop controller.

### 3.4. Wind turbine controller

The wind turbine has two control strategies: in one, rotor speed and blade pitch are constant and prescribed in an open-loop fashion; in the other, generator torque and collective-blade pitch are changed dynamically with the Reference Open-Source Controller (ROSCO) presented in [33,34] based on feedback of generator speed and measurement of wind speed. The ROSCO has region-based control strategies that maximize power production in below rated wind speeds and regulate rotor speed by means of collective blade pitch in above rated wind speeds. The overall structure of the controller and its integration in the experimental setup is shown in Fig. 4.

The generator torque and blade pitch controllers are proportional–integral (PI) controllers. The control output  $y$ , generator torque in below rated and collective blade in above rated, is computed as:

$$y = k_{p,y}(\omega_{g,s} - \omega_g) + k_{i,y} \int_0^T (\omega_{g,s} - \omega_g) dt, \quad (12)$$

where  $y$  is the control input,  $k_{p,y}$  and  $k_{i,y}$  are the proportional and integral gains,  $\omega_g$  is generator speed, and  $\omega_{g,s}$  is the generator speed set point. Below rated, blade pitch is equal to 0°, and the generator speed setpoint is:

$$\omega_{g,s} = \tau_g \frac{\lambda_0 \hat{u}}{R}, \quad (13)$$

where  $\lambda_0 = 9$  is the tip-speed ratio that is tracked to maximize the power coefficient,  $\hat{u}$  is the hub-height wind speed measured by the



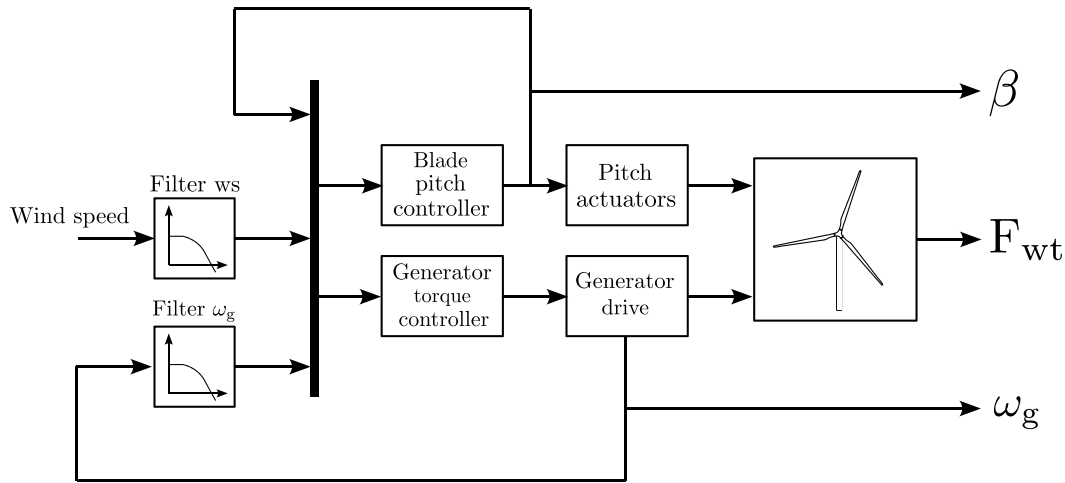


Fig. 4. Block diagram showing the wind turbine controller. “Filter ws” is the low-pass filter for wind speed, “Filter gs” is the low-pass filter for generator speed,  $\omega_g$  is the generator speed signal from the generator encoder,  $F_{wt}$  is the 6-components force measured by the tower-top load cell,  $Q_g$  is the generator torque,  $\beta$  is the collective blade pitch.

upstream pitot tube,  $R$  is the rotor radius, and  $\tau_g$  the gearbox ratio. Above rated, the generator torque is constant and equal to:

$$Q_g = \frac{P_0}{\eta_g \tau_g \omega_{r,0}}, \quad (14)$$

where  $P_0$  is the rated power, and  $\omega_{r,0}$  the rated rotor speed. Collective blade pitch is computed with a PI controller as the one of Eq. (12), where the setpoint is  $\omega_{g,s} = \tau_g \omega_{r,0}$ .

The wind turbine controller is run at model scale to respect the time scaling of the experiment and is tuned with the approach of [4] to have at model scale the same aero-servo-dynamic response of the full-scale turbine. Floating wind turbines that use collective-blade pitch-to-feather control may suffer of the infamous negative damping problem due to the coupling of the blade pitch controller action with the low-frequency nacelle fore-aft motion associated to platform rigid-body modes [35,36]. To solve this issue, the blade pitch controller has a bandwidth lower than the natural frequency of the platform pitch mode. The same controller tuning is used for the Activefloat and the WindCrete.

#### 4. Load cases

Load cases include: (1) tests with wind and fixed tower bottom that are used to assess the steady-state response of the wind turbine with closed-loop control; (2) free-decay tests to evaluate the response of the platform surge and pitch rigid-body modes and how these are influenced by the HIL control system, by aerodynamic loading and by the wind turbine control strategy; (3) tests with wind and irregular waves to verify the floating turbine coupled response in realistic operating conditions.

Load cases with wind are run in empty-inlet configuration, wind speed is uniform across the wind tunnel section with max variation of 5% across rotor disk and turbulence intensity about 2%. The vertical profile of mean wind speed and turbulence intensity is shown in Fig. 5. The examined wind turbine operating conditions are four, two below and two above the rated wind speed. Wind speeds and average values of rotor speed and blade pitch that defines the four operating states are reported in Table 4.

Tests with waves consider one irregular wave realization in which the propagation direction is parallel to the platforms main axis and to wind (when present), the wave spectrum is the JONSWAP with significant height  $H_s = 5.11$  m and peak period  $T_p = 9$  s, the duration is 5000 s. The scope of tests with irregular waves is to study the coupled response between platform motion and rotor. Tests with imposed motion have shown the coupling is maximum for surge and

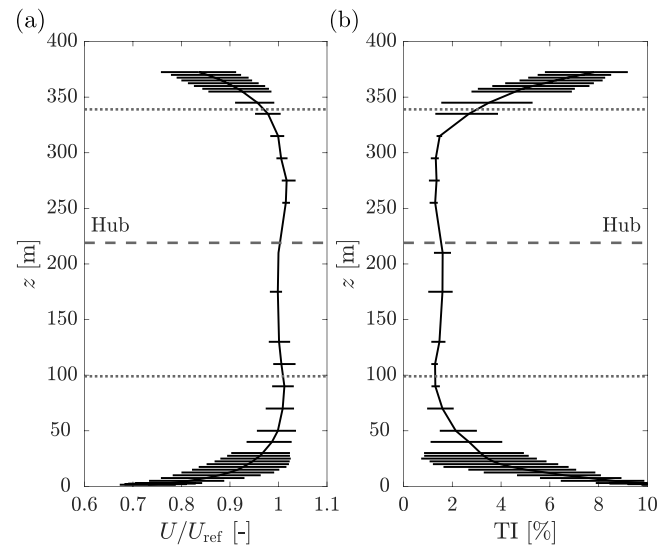


Fig. 5. Wind vertical profile at the wind turbine scale model location. (a) Mean wind speed ( $U$ ) normalized by its value at 100 m height ( $U_{ref}$ ). (b) Turbulence intensity (TI). Whiskers show the min/max across the wind tunnel cross section. The wind tunnel floor is at  $z = 0$ . The horizontal dashed lines are in correspondence of the turbine hub, the dotted lines mark the rotor edges.

Table 4  
Wind turbine operating conditions.

Condition	Wind speed [m/s]	Rotor speed [rpm]	Blade pitch [°]
BR1	9.0	6.6	0.00
BR2	9.6	7.4	0.24
AR1	13.1	7.6	8.60
AR2	17.3	7.6	14.64

pitch motion [3]. Hence, the condition with aligned waves is selected because it is associated with the largest excitation of the platform surge and pitch modes. The wave realization is the same in every load case to avoid uncertainty due to statistical variability of waves.

#### 5. Results

Results include: (1) verification of the steady-state turbine response with closed-loop control and fixed tower bottom; (2) platform response

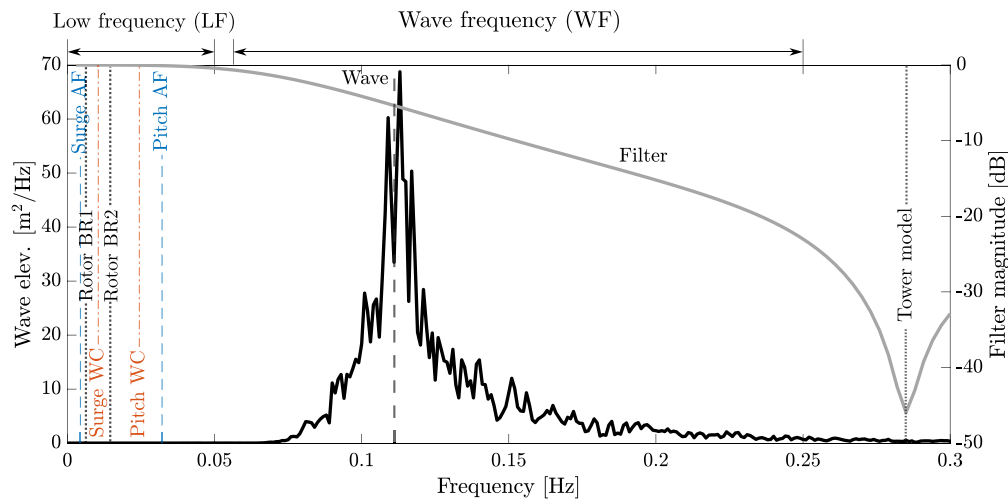


**Fig. 6.** Main frequencies of the experiment. The natural frequencies of the platform surge and pitch modes of the Activefloat (AF) and WindCrete (WC) are marked by gray lines. “Rotor” is the main frequency of rotor speed oscillations in below-rated wind cases. “Wave” is the spectrum of wave elevation in tests with stochastic waves. “Filter” is the magnitude of the filter of the hardware-in-the-loop force feedback. “Tower model” is the first fore-aft natural frequency of the physical wind turbine scale model. Analysis of experimental results makes reference to low-frequency (LF) and wave-frequency (WF) range.

with no wind for verification of the HIL system; (3) global FOWT response with wind and waves.

Fig. 6 shows the key spectral locations that are mentioned in the analysis of results. Colored vertical lines mark the position of the surge and pitch modes of the Activefloat (AF) and WindCrete (WC). The low-frequency range (LF), from 0 to 0.05 Hz, includes the platforms rigid-body modes. The wave-frequency range (WF), from 0.055 to 0.25 Hz, captures the frequency band where the magnitude of the wave spectrum is large. In the below-rated wind speed conditions, rotor speed shows oscillations (peak-to-peak amplitude of about 1 rpm) that are presumably due to rotor imbalance and are equally present with fixed and floating foundations. The frequency of these oscillations is marked with vertical dotted lines labeled “Rotor”. The oscillations are not seen in the above-rated region.

Fig. 6 also shows the filter of the HIL force feedback reported at full scale. The filter passes force signals in the LF range and attenuates their harmonics with higher frequency. The notch filter is visible in correspondence of the first fore-aft frequency of the turbine scale model, marked as “Tower model”.

### 5.1. Fixed turbine response

Before running load cases with floating foundations, the wind turbine response is measured at several wind speeds with fixed tower bottom. Fig. 7 shows the steady-state characteristics of wind speed-rotor speed-blade pitch-thrust-torque. When the turbine is controlled with the ROSCO (CL), rotor speed and blade pitch are outputs of the experiment and object of verification; otherwise with open-loop control (OL) rotor speed and blade pitch are fixed to the values of Table 4 according to mean wind speed, and rotor loads are the only outputs of the experiment. Experimental measures are compared to the IEA 15 MW and to predictions of the OpenFAST model of the scaled turbine, that is controlled with the same controller of the experiment. The OpenFAST model is believed to predict with good accuracy the steady-state response of the scaled turbine. Hence, large deviations of the experimental results from this model are symptom of an unwanted behavior of the scaled turbine.

With CL control, the rotor speed characteristic of the IEA 15 MW is matched with good accuracy and the amount of blade pitch required to do so is the same as for the reference wind turbine. Rotor thrust is reproduced well in BR1, that is the operating condition considered for aerodynamic design of the scaled blade. Scaling of rotor torque is not the primary objective of the blade design, and in below-rated wind

the aerodynamic torque of the scaled turbine is below the reference curve, but in line with the OpenFAST model. With this last observation it is possible to say the turbine scale model behaves according to the assumptions used for blade and controller design.

In the above-rated region, rotor torque has its rated value, and the turbine scale model produces the rated power. The correct torque is achieved at the expense of a thrust force higher than for the IEA 15 MW. This behavior is also seen in the OpenFAST model, but values of rotor thrust measured in the wind tunnel are higher than in simulations (the difference increases with wind speed and it is 12% at 23 m/s). Since the rotor speed and blade pitch characteristics of the experiment are in line with OpenFAST, this difference is attributed to the 2D polars that are used inside the OpenFAST aerodynamic model.

Tests with CL and the wind conditions of Table 4 are repeated three times to check their repeatability. Dispersion of all metrics is low in BR1, AR1 and AR2. The highest variability is seen in BR2 wind, which is close to the rated condition, and the effect is more evident in rotor torque than in any other output. The low dispersion of results in above-rated wind is obtained paying particular attention to the blade pitch angle setting, that was supposed to be the main source of uncertainty for the turbine response in [3,4]. The dispersion in BR2 is attributed to the CL controller that has to switch from partial-load to full-load operation. Dispersion of results in this condition may be reduced using a set point smoothing strategy as the one described in [33].

### 5.2. Verification of the HIL system with no wind

The coupling of the physical and numerical subdomains realized by the HIL system must be transparent, i.e. it must not influence the physics of the FOWT. In other words, the response of the FOWT should be due to the phenomena modeled in the wind tunnel and in the hydrodynamic model, but not due to the mathematics introduced in Section 3.1. Transparency is verified with tests in still air where the force feedback is alternatively disabled ( $F_{wt,n} = 0$ ) or active (it is computed with Eq. (2)). Since there is no wind, aerodynamic forces are negligible, rotor loads are mainly due to weight and inertia, and it is expected that  $F_{wt,n} \approx 0$ . Hence, the FOWT response should be the same with disabled or active HIL.

The first verification is done in free decay tests for the surge and pitch motion. Fig. 8 shows the time series of decay tests for the two FOWTs, where the initial displacement is imposed alternatively on the platform surge or pitch DOF. By eye inspection, the HIL does not appear to affect FOWT motion much. The impact is quantified comparing the

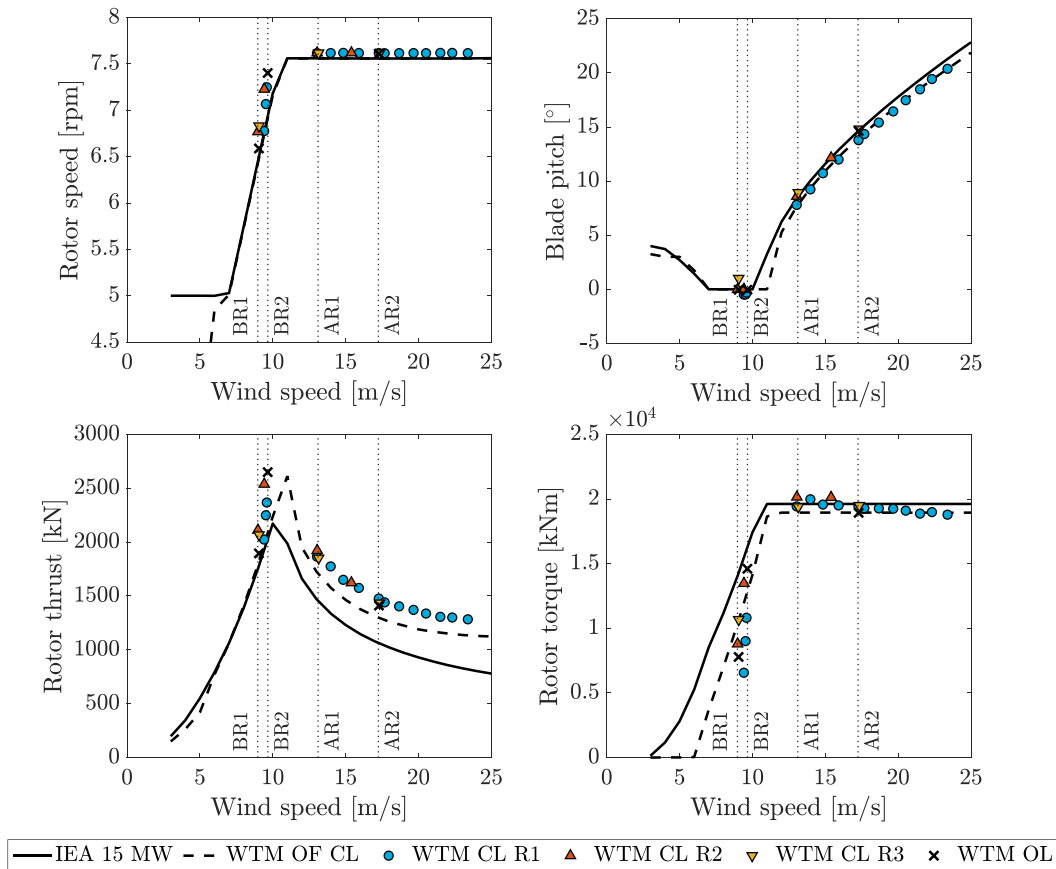


Fig. 7. Steady state response of the wind turbine scale model (WTM) compared to the IEA 15 MW. R1, R2, and R3 are repeated measurements of the response with closed-loop control (CL), OL is open-loop control, “OF” is the OpenFAST simulation of the turbine scale model. The vertical dotted lines mark the operating conditions of Table 4.

Table 5

Natural period ( $T_n$ ) and damping ratio ( $\xi$ ) for the platform surge and pitch modes of the Activefloat and WindCrete obtained from free decay tests of Fig. 8. When HIL is “Active” the force feedback to the numerical model is enabled, otherwise it is turned off.

FOWT	DOF	HIL	$T_n$ [s]	$\xi$ [%]
Activefloat	Surge	No	231.55	7.64
Activefloat	Surge	Active	225.48	6.67
Activefloat	Pitch	No	32.64	4.10
Activefloat	Pitch	Active	31.71	4.29
WindCrete	Surge	No	82.97	9.44
WindCrete	Surge	Active	81.83	7.61
WindCrete	Pitch	No	42.87	4.01
WindCrete	Pitch	Active	42.06	3.15

natural period and damping ratio that are computed from the free-decay time histories with the logarithmic decrement method and are reported in Table 5. The variation of natural period with active HIL is below 3% for all cases and is deemed negligible. Damping ratio is slightly decreased with HIL compared to the case without force feedback and the maximum decrement is  $-1.8\%$  for the WindCrete surge mode. A damping decrement due to HIL is found also in [20] and is similar in value to that of this work.

Transparency of the HIL system is verified also with irregular waves, which provide excitation in a broad frequency range. Fig. 9 shows the time series of platform surge and pitch motion of the two FOWTs, with and without force feedback. The effect of HIL activation on the quality of motion is quantified as the root mean square error (RMSE) between the motion of one platform DOF with HIL and without it. The RMSE for surge is 0.14 m for the Activefloat and 0.61 m for the WindCrete, the RMSE for pitch is  $0.02^\circ$  for the Activefloat and  $0.15^\circ$  for the WindCrete.

Table 6

Integral of the power spectral density of three different metrics in tests with irregular waves, no wind and different configurations of the HIL system. The integral is evaluated in the low-frequency range (LF, 0–0.05 Hz) and in the wave-frequency range (WF, 0.055–0.25 Hz). In the “No HIL” configuration the force feedback of the HIL system is turned off, in “HIL” the force feedback is enabled.

FOWT	Metric	Unit	Freq. range	No HIL	HIL
Activefloat	Plat. pitch	$\text{deg}^2$	LF	$1.69 \times 10^{-3}$	$2.21 \times 10^{-3}$
Activefloat	Nac. acc.	$\text{m}^2/\text{s}^4$	LF	$1.98 \times 10^{-5}$	$2.75 \times 10^{-5}$
Activefloat	Tower-top Fx	$\text{N}^2$	LF	$3.68 \times 10^8$	$5.06 \times 10^8$
Activefloat	Plat. pitch	$\text{deg}^2$	WF	$5.33 \times 10^{-5}$	$5.82 \times 10^{-5}$
Activefloat	Nac. acc.	$\text{m}^2/\text{s}^4$	WF	$1.03 \times 10^{-2}$	$1.02 \times 10^{-2}$
Activefloat	Tower-top Fx	$\text{N}^2$	WF	$1.96 \times 10^{11}$	$1.93 \times 10^{11}$
WindCrete	Plat. pitch	$\text{deg}^2$	LF	$1.79 \times 10^{-2}$	$2.76 \times 10^{-2}$
WindCrete	Nac. acc.	$\text{m}^2/\text{s}^4$	LF	$2.92 \times 10^{-4}$	$3.96 \times 10^{-4}$
WindCrete	Tower-top Fx	$\text{N}^2$	LF	$4.00 \times 10^9$	$6.88 \times 10^9$
WindCrete	Plat. pitch	$\text{deg}^2$	WF	$9.92 \times 10^{-3}$	$1.12 \times 10^{-2}$
WindCrete	Nac. acc.	$\text{m}^2/\text{s}^4$	WF	$1.35 \times 10^{-1}$	$1.53 \times 10^{-1}$
WindCrete	Tower-top Fx	$\text{N}^2$	WF	$2.49 \times 10^{12}$	$2.80 \times 10^{12}$

The error introduced by HIL activation on platform motion is small and slightly larger for the WindCrete compared to the Activefloat.

The power spectral density (PSD) of the time histories of Fig. 9 helps to understand how the HIL affects the FOWT response at the different frequencies. The PSDs are reported in Fig. 10. The main differences are seen in proximity of the peaks of the platform surge and pitch modes; the frequency of peaks is the same with and without HIL, whereas their amplitude is higher in the case with HIL. This is in line with the results of free decay tests which have shown the HIL reduces damping of platform motion. The response in the wave frequency range is about the same with the two HIL configurations.



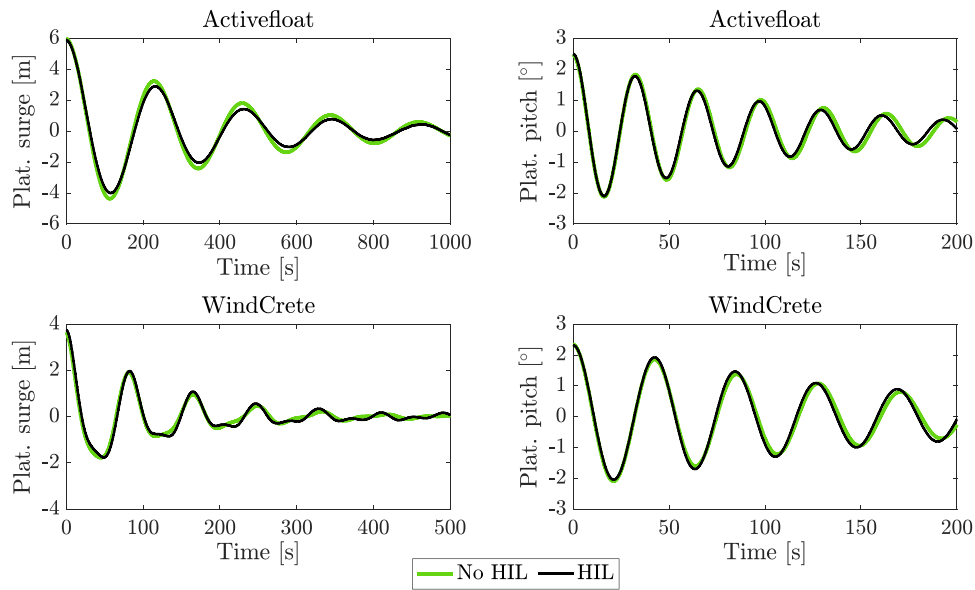


Fig. 8. Platform surge and pitch response in free decay tests with no wind and different configurations of the HIL system. In the “No HIL” configuration the force feedback of the HIL system is turned off, in “HIL” the force feedback is enabled.

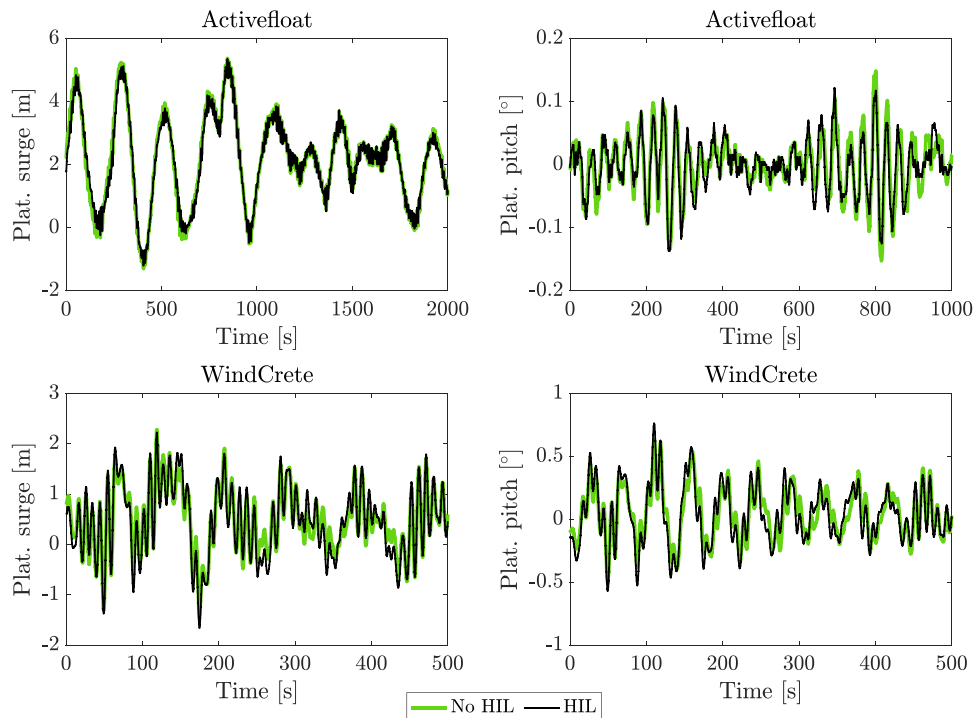


Fig. 9. Time series of the platform surge and pitch motion with irregular waves, no wind and different configurations of the HIL system. In the “No HIL” configuration the force feedback of the HIL system is turned off, in “HIL” the force feedback is enabled. The insets show the wave-frequency range.

The influence of HIL is further studied computing the integral of the PSD of platform pitch motion, nacelle acceleration in the  $x$ -axis of CS3, and tower-top force along the  $x$ -axis of CS2. The PSD integral is computed in the LF range and in the WF range. Results are reported in Table 6: integrals in the WF range are mostly unaltered with HIL compared to the case with zero force feedback. Nacelle acceleration in the WF range is about three orders of magnitude greater than in the LF range; tower-top loads follow the same trend, because in the WF range they are dominated by inertia forces. Despite this large loads, the FOWT motion is consistent with and without HIL and this proves the force feedback estimation discussed in Section 3.1 is effective in removing

inertia and weight loads. Small variations of the PSD integrals are seen in the LF range; the FOWTs motion is slightly increased with HIL due to decreased damping of platform modes. The consequence of the larger motion and nacelle acceleration is an increment in tower-top forces.

Concluding the HIL verification analysis, we see the system is mostly transparent and does not influence the response of the FOWTs in a meaningful way. There is some inaccuracy in the force feedback whose effect on the FOWT response can be explained in two ways, that are exemplified in Fig. 11. The force feedback  $F_{wt,n}$  has inside part of the rotor-nacelle inertia, that is not completely removed with the force subtraction of Eq. (2). This force is visualized on the left of Fig. 11:

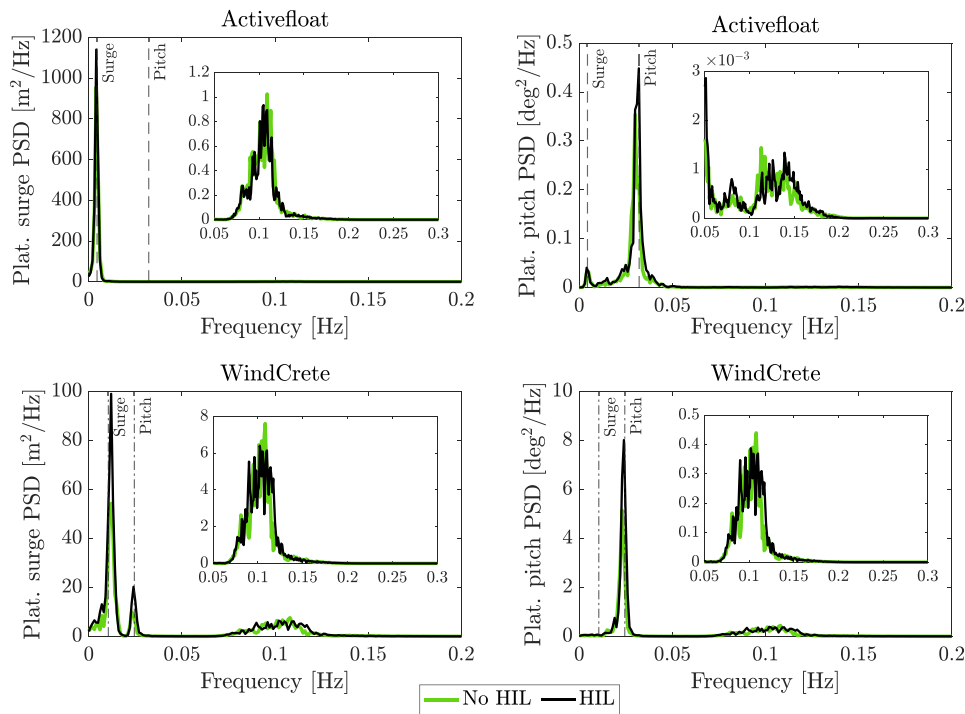


Fig. 10. Power spectral density of the platform surge and pitch motion with irregular waves, no wind and different configurations of the HIL system. In the “No HIL” configuration the force feedback of the HIL system is turned off, in “HIL” the force feedback is enabled. The insets show the wave-frequency range.

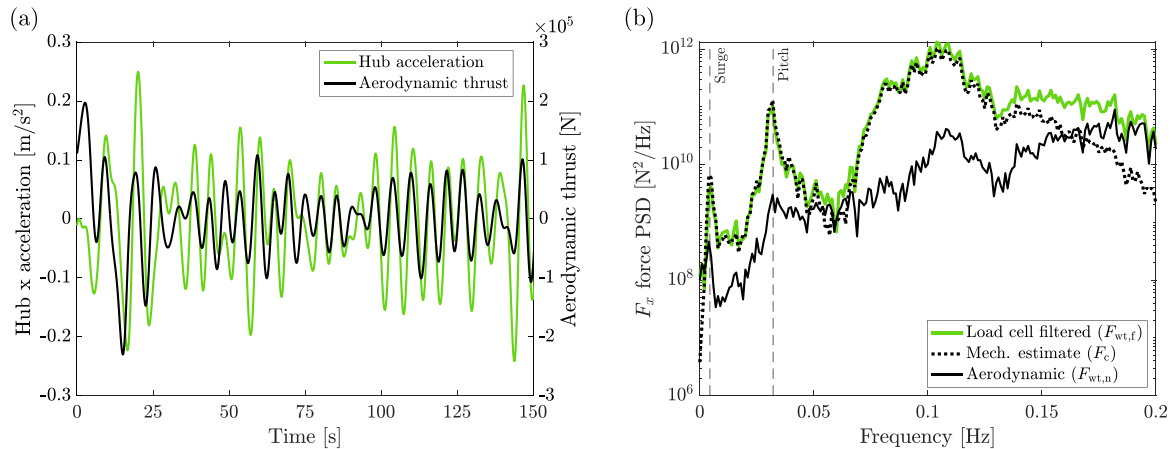


Fig. 11. Thrust force feedback of the HIL with irregular waves and no wind. (a) Thrust force and hub acceleration. (b)  $F_x$  force components in the HIL control system of Fig. 3.

the component in phase with acceleration (e.g., visible at 100–125 s) acts as an additional mass, the part in phase with velocity as damping. Decays show the period of platform modes does not change and mass variation due to this force is negligible; the small change in damping can be attributed to the residual inertia force in phase with velocity. The PSD of the  $x$  component of  $F_{wt,f}$ ,  $F_c$  and  $F_{wt,n}$  is shown in Fig. 11.  $F_{wt,f,x}$  is large in correspondence of the natural frequencies of its rigid body modes where large nacelle motion is caused by resonance, and in the WF range. In correspondence of the platform modes  $F_{c,x} \approx F_{wt,f,x}$  but the residual  $F_{wt,n,x}$  excites the system in resonance, causing the increased amplitude of response at these frequencies.

### 5.3. Response to wind and irregular waves

The mutual influence of wind loads, wind turbine control strategy and hydrodynamic loads on the response of the Activefloat and WindCrete is studied with load cases combining the same irregular wave of Section 5.2 with the four wind conditions of Table 4.

The PSD of platform surge and pitch motion with different wind conditions, with OL and CL control, is shown in Fig. 12 for the Activefloat and in Fig. 13 for the WindCrete. The maximum amplitude of motion is in correspondence of the platform natural frequencies as with no wind. With OL control and any wind condition, the PSD amplitude at the platform modes is lower than in still air and this behavior is the same for the two FOWTs. With CL control, the amplitude of platform motion in the LF range is higher or lower than with no wind depending on the turbine operating condition. The amplitude of surge motion of the Activefloat is increased in BR1 compared to still air due to variations of rotor thrust caused by rotor speed oscillations which are close in frequency to the Activefloat surge mode (see Fig. 6) In BR2 wind, the effect of CL control on the two FOWTs is to increase the amplitude of motion, up to 10 times compared to the no wind case, instead of reducing it as with the OL control. With AR2 wind, the amplitude of platform pitch motion is similar to the no wind case. The platform motion in the WF range is the same for any wind condition

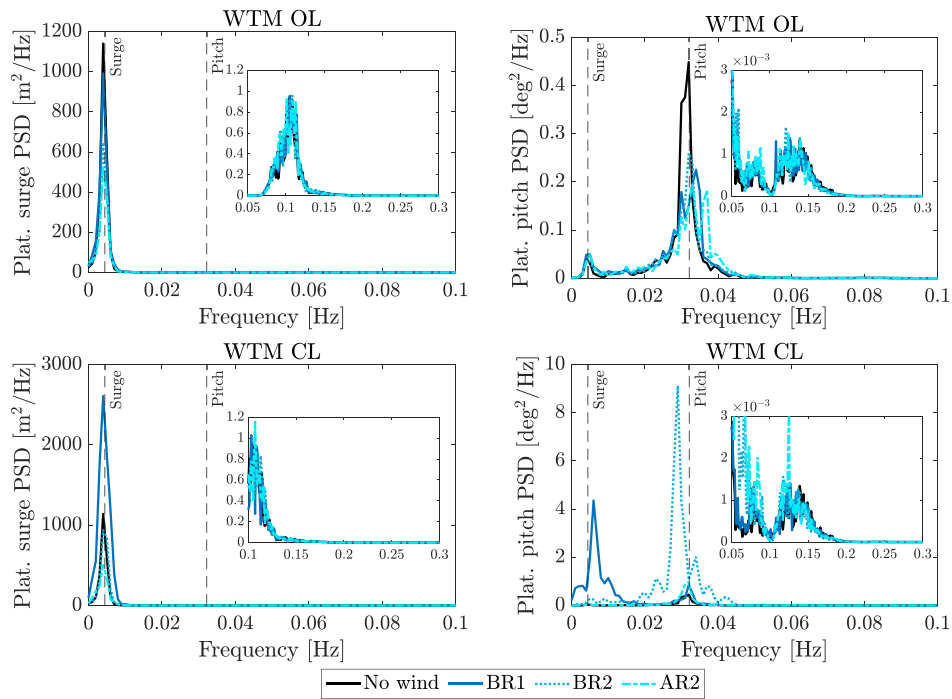


Fig. 12. Power spectral density of the platform surge and pitch motion for the Activefloat with different wind conditions, with closed-loop wind turbine control (“WTM CL”) or fixed rotor speed and blade pitch (“WTM OL”). The insets show the wave-frequency range.

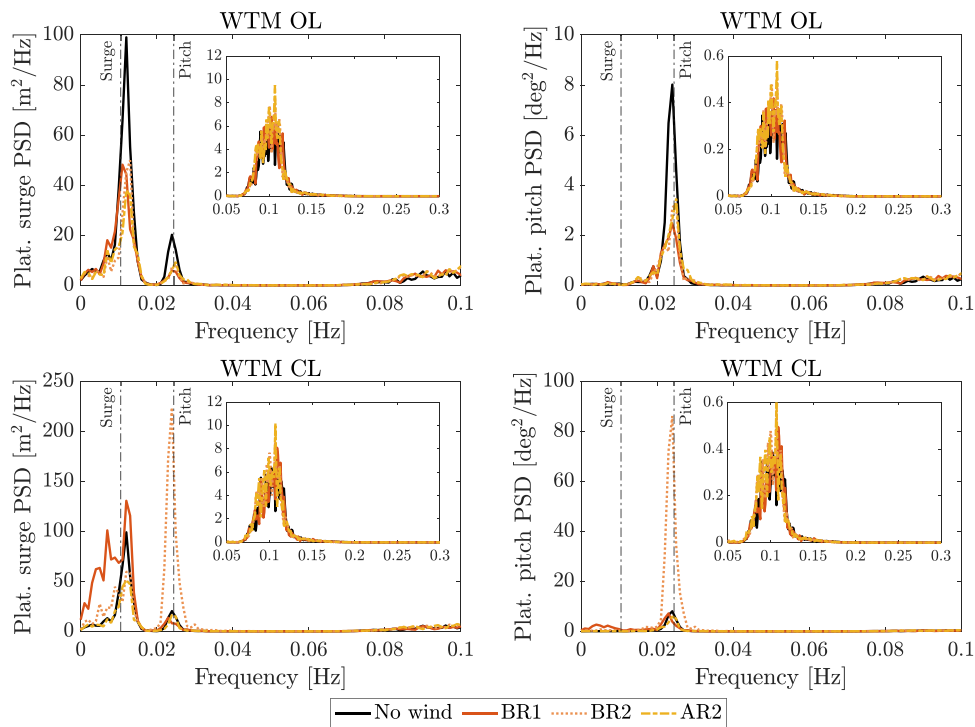


Fig. 13. Power spectral density of the platform surge and pitch motion for the WindCrete with irregular waves and different wind conditions, with closed-loop wind turbine control (“WTM CL”) or fixed rotor speed and blade pitch (“WTM OL”). The insets show the wave-frequency range.

and wind turbine control strategy. In this frequency range, linear wave loads are the dominant source of excitation for the platform and, at the same time, aerodynamic loads are mitigated by the low-pass filter of the HIL system.

The rotor response with CL control is examined in Fig. 14, which shows the PSD of rotor speed, generator torque and collective blade pitch. Rotor speed and generator torque have oscillations at 0.006 Hz in

BR1 and at 0.014 Hz in BR2, which are present also when tower bottom is fixed. These oscillations are attributed to mechanical imbalance of the rotor and of the belt connecting the low-speed and high-speed shafts in the turbine scale model. Rotor speed oscillations cause dynamic thrust variations that excite the platform response. In BR1, rotor speed oscillations excite the surge mode of the Activefloat causing the peak in the PSD of platform surge in Fig. 12. Rotor speed oscillations in BR2

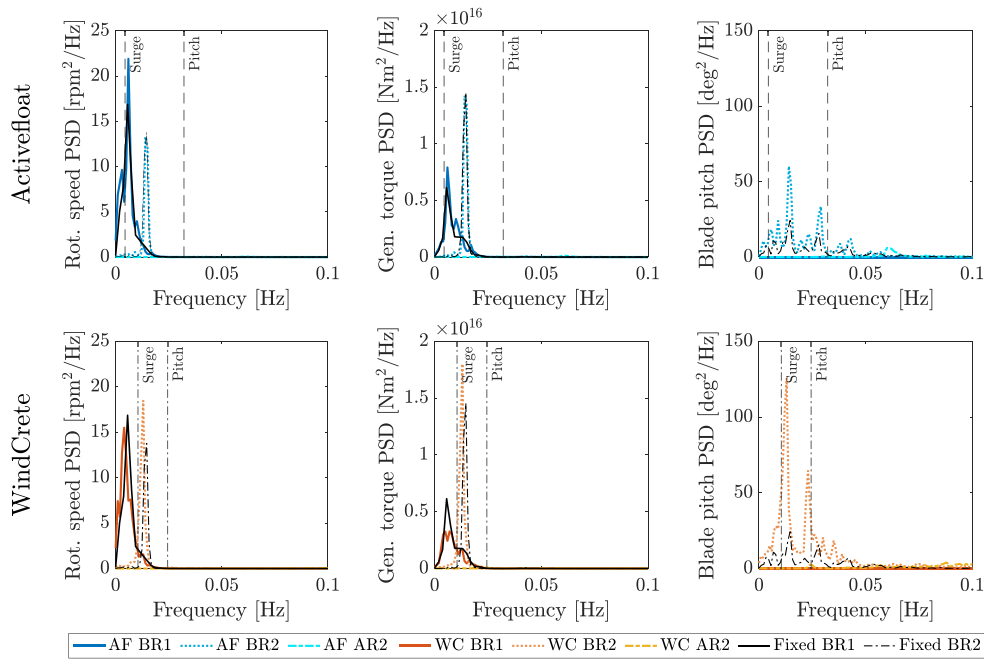


Fig. 14. Power spectral density of rotor speed, generator torque and collective blade pitch for the Activefloat and WindCrete with irregular waves, different wind conditions and closed-loop wind turbine control.

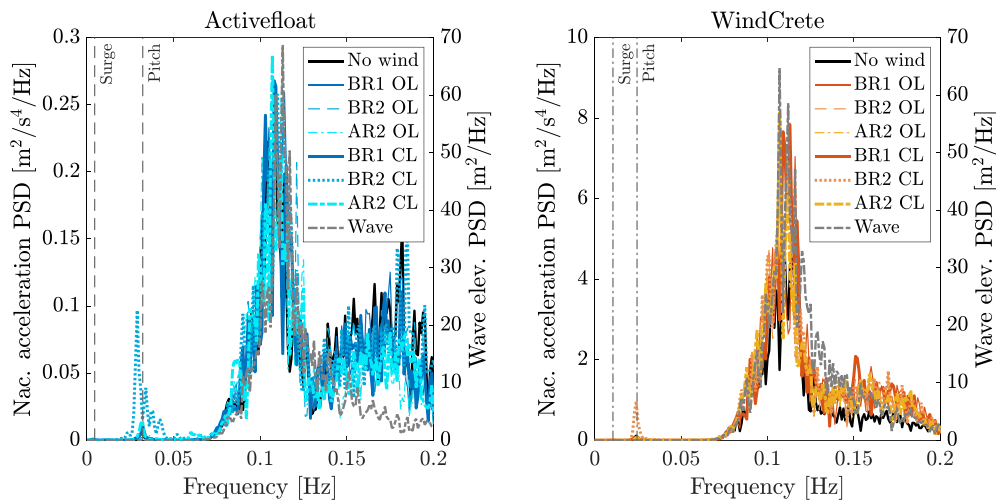


Fig. 15. Power spectral density of nacelle acceleration in the x-axis of CS3 for the Activefloat and WindCrete with irregular waves and different wind conditions, with closed-loop wind turbine control (CL) or fixed rotor speed and blade pitch (OL). “Wave” is the power spectral density of wave elevation.

are close in frequency to the surge mode of the WindCrete, but are not followed by a peak in the PSD of platform surge motion.

The BR2 condition is very close to the rated wind speed, and blade pitch is activated by the wind turbine controller. The blade pitch activity for the Activefloat and WindCrete is increased with respect to the bottom-fixed case: the PSDs have a first spike at the frequency of rotor speed oscillations, and one at the platform pitch frequency. The latter demonstrates the coupling between the platform pitch response and blade pitch actuation. An increase of rotor speed oscillations and platform motion is also found in the wave basin experiments of a 10 MW tension-leg platform of [12], with above rated wind and irregular waves. The increase of platform pitch motion in BR2 wind is attributed to the action of the CL controller. Even if the controller bandwidth is lower than the platform pitch frequency and the FOWT response is stable, the active blade pitch controller reduces the damping of the platform pitch mode. On the contrary, with fixed-pitch control there is no coupling between the rotor and platform response, and damping

is increased. An analogous result is found in the wave basin experiment of [10] with similar control configurations. In [10] the increased pitch motion is found for a wind condition in between our AR1 and AR2, but there are no results for near-rated wind.

The PSD of nacelle acceleration for the load cases with wind is reported in Fig. 15. The largest peak is in the WF range and it is due to linear wave loads, as it is possible to deduce comparing the spectra of acceleration and wave. Acceleration in the WF range with no wind is highly similar to cases with wind; some differences are seen above 0.12 Hz, where the PSD amplitude of the Activefloat is slightly lower compared to the no wind case, and for the WindCrete it is slightly higher. In the LF range, there is a peak in correspondence of the platform pitch mode of the two FOWTs, which is present only in BR2. Resonant platform pitch motion causes large variations of nacelle acceleration and, since it is at low frequency, large oscillations of the apparent wind seen by rotor. The blade pitch controller responds to this dynamic wind speed.

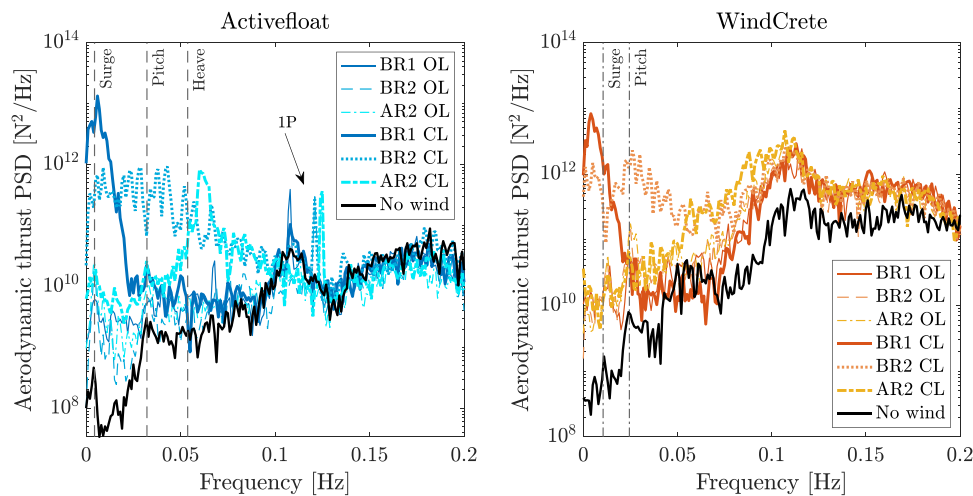


**Fig. 16.** Power spectral density of aerodynamic thrust force  $F_{wt,n,x}$  for the Activefloat and WindCrete with irregular waves and different wind conditions, with closed-loop wind turbine control (“CL”) or fixed rotor speed and blade pitch (“OL”). Notice this is the estimated aerodynamic thrust computed by the HIL control system; in the “No wind” case it is the inertia and weight loads that are not completely removed in the force subtraction. The arrow with label “1P” points to the peak associated with one-per-revolution oscillations due to rotor aerodynamic imbalance.

The PSD of the aerodynamic thrust force  $F_{wt,n,x}$ , which is fed back to the numerical model, is shown in Fig. 16. In the Activefloat case, the thrust force in the WF range is about the same with any wind condition and wind turbine control strategy, and it is close to the no wind case. In this frequency range, the thrust force is mostly due to inertia that is not removed in the force subtraction. The differences with respect to the no wind case are: (1) above 0.12 Hz the force is slightly lower with wind, and this explains the decreased amplitude of nacelle acceleration; (2) there is a peak at the rotor one-per-revolution frequency (1P) that is caused by rotor aerodynamic imbalance, and it is the same with OL and CL. In the WindCrete case, the thrust force in the WF range is higher with wind than with still air, and this explains the higher amplitude of nacelle acceleration. The 1P peak is not as visible, and is likely hidden.

The strong coupling between aerodynamic and hydrodynamic response can be appreciated in the LF range, and almost the same behavior is seen for the two FOWTs. With OL, the thrust force is increased with respect to when the turbine is not spinning, the additional force is about the same independently of the wind condition, and damps the platform motion. With CL, the LF aerodynamic thrust is sensitive to the wind condition. In BR1, there is a peak at 0.006 Hz that is due to the already commented rotor speed variations. In BR2 wind, the spectrum amplitude is increased across the entire LF range, and in the WindCrete case it is possible to distinguish a broad peak near the platform pitch frequency, that is not evident in the Activefloat. In AR2 wind, the thrust amplitude in the LF is lower and comparable to the cases with OL, but it is still possible to distinguish a peak at the platform pitch frequency. In the Activefloat case, there is broad peak near the platform heave frequency that is not present in any other case.

#### 5.4. Aerodynamic damping of platform pitch

To better understand the coupled response of rotor aerodynamics and low-frequency platform motion, free decay tests are conducted with different wind conditions and the two turbine control strategies.

In Fig. 17 we examine the platform surge and pitch motion in surge and pitch decays with different wind conditions and CL control. The figure shows AR cases because blade pitch is not saturated and it is easier to see the coupling between platform motion and controller response. In surge decays, the coupling of platform motion with rotor is weak, rotor speed and blade pitch are about constant and do not show any visible trace of the FOWT movement. In pitch decays, rotor speed and blade pitch exhibit large amplitude oscillations with the same frequency of platform pitch. The oscillations of platform pitch

have the same amplitude in AR1 and AR2, but blade pitch variations are larger at the lower wind speed. The Activefloat and WindCrete share the same behavior.

The platform surge mode has weak coupling with rotor, whereas the platform pitch mode of the Activefloat and WindCrete is strongly coupled with rotor. The platform pitch response in free-decay tests in the pitch direction is analyzed to quantify the amount of damping introduced by aerodynamic rotor loading with OL and CL control. The total damping, hydrodynamic and aerodynamic, for the two FOWTs is reported in Fig. 18a. With OL control, damping in any wind condition is higher than in still air. With CL control, damping is higher than in no wind in BR1 and BR2, and lower in AR1 and AR2.

A simple analytical model to understand the influence of wind and turbine control on the platform damping is described in [37] for a 5 MW tension-leg platform FOWT. The model considers only the platform pitch DOF and shows that, when platform motion is slow, the aerodynamic damping is proportional to the derivative of the aerodynamic thrust with respect to wind speed. This derivative is evaluated in two ways. One way is to compute the derivative of the steady-state wind speed-thrust characteristic of Fig. 7: this derivative represents the sensitivity to wind speed variations with closed-loop control. The second way is to calculate the variation of thrust force due to a change in wind speed, with constant rotor speed and blade pitch: this way of computing the thrust derivative characterizes the sensitivity with open-loop control.

The aerodynamic damping is estimated subtracting the value with no wind from results of Fig. 18a. The result is reported in Fig. 18b, where it is compared to the open-loop and closed-loop derivatives of thrust. The aerodynamic damping with CL control increases with wind speed up to rated where it is largest in magnitude; it changes sign for higher wind speeds, it is minimum in AR1 and increases slightly in AR2, like the closed-loop derivative of thrust. The open-loop thrust derivative increases with wind speed in below rated; it is about flat and positive above rated, and the trend is similar to the aerodynamic damping with OL control. These results are in line with those of [37], that were obtained with numerical simulations.

The aerodynamic damping in free-decay tests is compared to the integral of the power spectral density of platform pitch motion with irregular waves, which is reported in Fig. 19. Figs. 12–13 show that platform pitch motion with irregular waves is dominated by the response at the pitch natural frequency. Aerodynamic damping has an impact on the amplitude of the resonant pitch motion, whereas the wave frequency response is the same regardless of the wind condition



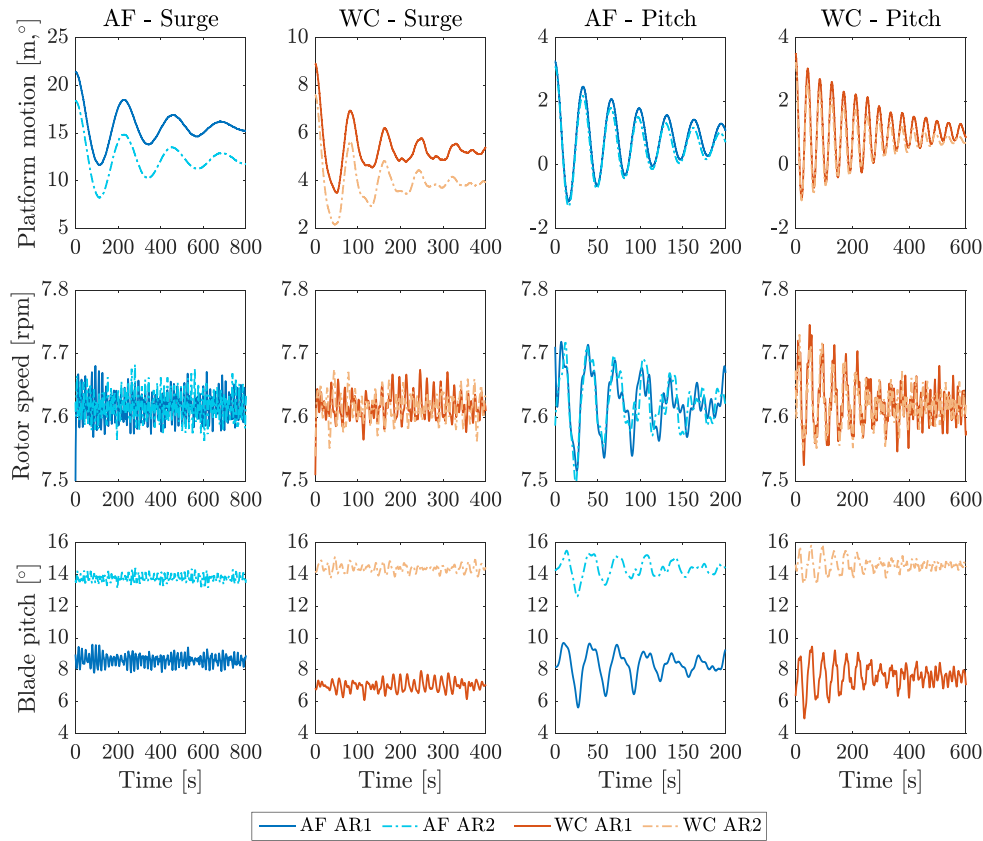


Fig. 17. Platform and rotor response of the Activefloat (AF) and WindCrete (WC) in free decay tests with two above-rated wind conditions. The wind turbine has closed-loop control.

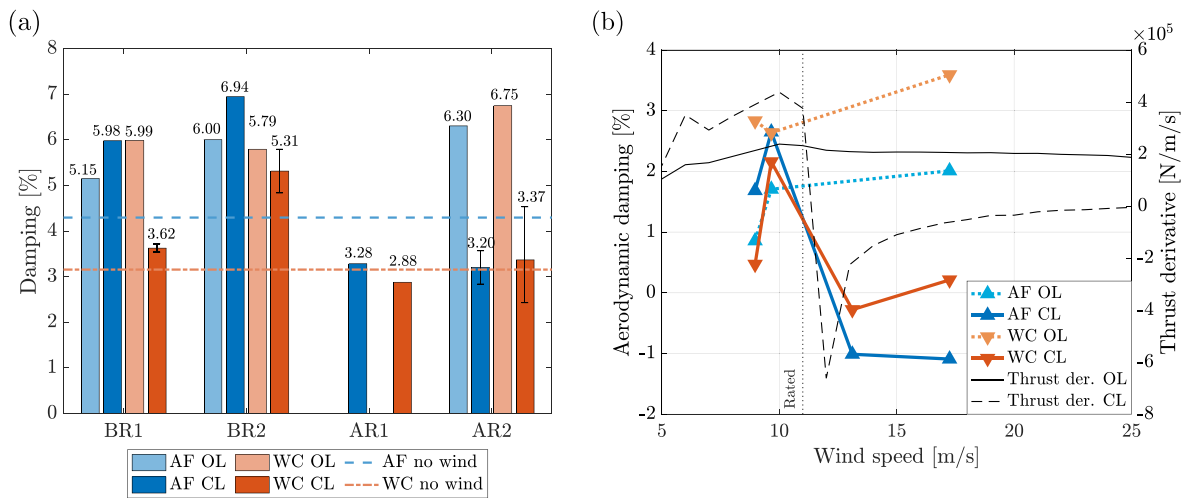


Fig. 18. Damping of the platform pitch mode for the Activefloat (AF) and WindCrete (WC) obtained in free-decay tests with different wind turbine operating conditions, with closed-loop wind turbine control (CL) or fixed rotor speed and blade pitch (OL). (a) Damping ratio (total of hydrodynamic and aerodynamic). (b) The amount of damping due to aerodynamic loading is compared to derivatives of thrust force. The OL derivative is the thrust variation due to apparent wind, with constant rotor speed and blade pitch; the CL derivative is the derivative with respect to wind speed of the steady-state thrust characteristic of Fig. 7.

and wind turbine control strategy. The amplitude of low-frequency platform pitch deviations with OL control is constant for any wind condition and is slightly lower than with no wind. This is in accordance with the trend of aerodynamic damping in free decays, that is about constant for any wind condition and higher than with no wind. With CL control, the platform pitch LF-PSD integral increases passing from

BR1 to BR2, it is minimum in AR2 where it is similar to the no wind case. Although there is no results for AR1, we see there are some differences between the trend of aerodynamic damping and the low-frequency PSD in irregular waves: the LF-PSD in BR1 is higher than in AR2, whereas pitch damping in free decays is higher in BR1 than in AR2; the LF-PSD increases passing from BR1 to BR2, whereas damping

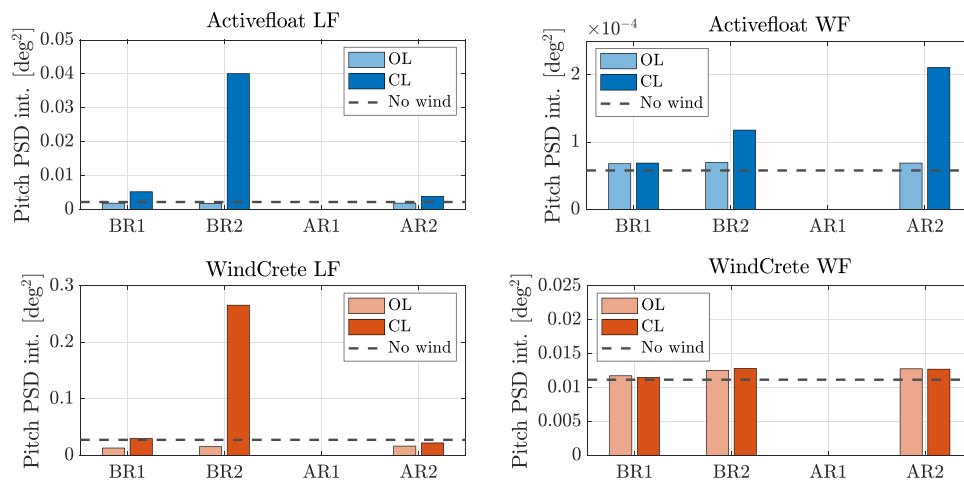


Fig. 19. Integral of the power spectral density of platform pitch motion with irregular waves, different wind conditions, with closed-loop wind turbine control (“CL”) or fixed rotor speed and blade pitch (“OL”), in the low-frequency range (LF) and wave-frequency range (WF).

increases according to free decay tests. This difference in the platform pitch response with CL control is attributed to the non-linearity of the coupled aero-hydro-servo-dynamic response of the system. The pitch response in irregular waves is worth investigating further and verifying that it is captured correctly in offshore codes.

## 6. Conclusions

In this article we presented the methodology and results of a wind tunnel experiment using HIL to model the coupled aero-hydro-servo-dynamic of two 15 MW floating wind turbines, a spar and a semi-submersible. The experiment emulated the IEA 15 MW turbine with a 1:100 scale model that has a performance-scaled rotor and reference closed-loop control functionalities. The platform hydrodynamics and rigid-body response is simulated with a numerical model that is integrated in run time, and it is coupled with the physical part of the experiment by means of force feedback and tower-base motion control.

Before tests with wind and waves, verification tests are run to assess the steady-state performance of the wind turbine with fixed tower-base. The scaled wind turbine reproduces with good accuracy the rotor speed-blade pitch-thrust-torque characteristics of the IEA 15 MW. Deviations from reference are seen for rotor torque in below-rated wind, and for rotor thrust in above-rated wind because matching of this quantities is outside the objectives of rotor aerodynamic design.

The two floating wind turbines are tested with various wind speeds and two different turbine control strategies. When the wind turbine is controlled with fixed rotor speed and blade pitch, the rotor aerodynamic loads increase the damping of platform modes, reducing the low-frequency motion of the structure. In this control configuration, aerodynamic damping is nearly constant and shows little dependence on wind speed. With closed-loop wind turbine control, aerodynamic damping is higher than in no wind when the turbine operates below the rated wind speed, but it is lower for higher wind speeds. The minimum damping is in proximity of the rated condition. Variations of damping are due to the coupling of the platform pitch mode with the rotor response and wind turbine controller action, and results are consistent for the WindCrete and Activefloat.

The present paper shows that HIL wind tunnel testing is a valuable tool to investigate the coupled response of floating wind turbines in a laboratory environment. In future works, measurements of wind turbine quantities collected in this experiment can be used for validation of aerodynamic calculations in offshore codes considering conditions close to those faced by floating wind turbines in normal operation. This synergistic combination of experimental testing and numerical simulation tools can help reduce the cost of floating wind energy and enable its rapid growth.

## CRedit authorship contribution statement

**Alessandro Fontanella:** Conceptualization, Methodology, Software, Validation, Formal analysis, Writing – original draft, Writing – review & editing. **Alan Facchinetti:** Conceptualization, Methodology, Software, Validation, Writing – original draft, Supervision, Project administration. **Elio Daka:** Conceptualization, Software. **Marco Belloli:** Conceptualization, Methodology, Project administration, Funding acquisition.

## Declaration of competing interest

The authors declare that they have no known competing financial interests or personal relationships that could have appeared to influence the work reported in this paper.

## Acknowledgments

### Financial disclosure

This research has been supported by the Horizon 2020 (COREWIND (grant no. 815083)).

## References

- [1] S. Gueydon, I. Bayati, E.J. de Ridder, Discussion of solutions for basin model tests of FOWTs in combined waves and wind, *Ocean Eng.* 209 (2020) 107288.
- [2] A. Fontanella, I. Bayati, R. Mikkelsen, M. Belloli, A. Zasso, UNAFLOW: a holistic wind tunnel experiment about the aerodynamic response of floating wind turbines under imposed surge motion, *Wind Energy Sci.* 6 (5) (2021) 1169–1190.
- [3] A. Fontanella, A. Facchinetti, S. Di Carlo, M. Belloli, Wind tunnel investigation of the aerodynamic response of two 15 MW floating wind turbines, *Wind Energy Sci.* 7 (4) (2022) 1711–1729.
- [4] A. Fontanella, E. Daka, F. Novais, M. Belloli, Controller design for model-scale rotors and validation using prescribed motion, *Wind Energy Science* (9) (2023) 1351–1368.
- [5] F.G. Nielsen, T.D. Hanson, B. Skaare, Integrated dynamic analysis of floating offshore wind turbines, in: LNG Specialty Symposium of International Conference on Offshore Mechanics and Arctic Engineering, Volume 1, Offshore Technology; Offshore Wind Energy; Ocean Research Technology, 2006, pp. 671–679.
- [6] A.J. Goupee, B.J. Koo, R.W. Kimball, K.F. Lambrakos, H.J. Dagher, Experimental comparison of three floating wind turbine concepts 136 (2014) 020906.
- [7] A.N. Robertson, J.M. Jonkman, A.J. Goupee, A.J. Coulling, I. Prowell, J. Browning, M.D. Masciola, P. Molta, Summary of conclusions and recommendations drawn from the DeepCwind scaled floating offshore wind system test campaign, in: Ocean Renewable Energy of International Conference on Offshore Mechanics and Arctic Engineering, Volume 8, 2013, V008T09A053.

- [8] R. Kimball, A.J. Goupee, M.J. Fowler, E.-J. de Ridder, J. Helder, Wind/wave basin verification of a performance-matched scale-model wind turbine on a floating offshore wind turbine platform, in: *Ocean Renewable Energy of International Conference on Offshore Mechanics and Arctic Engineering*, Volume 9B, 2014, V09BT09A025.
- [9] A.J. Goupee, R.W. Kimball, H.J. Dagher, Experimental observations of active blade pitch and generator control influence on floating wind turbine response, *Renew. Energy* 104 (2017) 9–19.
- [10] H. Bredmose, F. Lemmer, M. Borg, A. Pegalajar-Jurado, R.F. Mikkelsen, T. Stoklund Larsen, T. Fjelstrup, W. Yu, A.K. Lomholt, L. Boehm, J. Azcona Armendariz, The Triple Spar campaign: Model tests of a 10MW floating wind turbine with waves, wind and pitch control, *Energy Procedia* 137 (2017) 58–76, 14th Deep Sea Offshore Wind R&D Conference, EERA DeepWind 2017.
- [11] W. Yu, F. Lemmer, H. Bredmose, M. Borg, A. Pegalajar-Jurado, R.F. Mikkelsen, T. Stoklund Larsen, T. Fjelstrup, A.K. Lomholt, L. Boehm, D. Schlipf, J. Azcona Armendariz, P.W. Cheng, The triple spar campaign: Implementation and test of a blade pitch controller on a scaled floating wind turbine model, *Energy Procedia* 137 (2017) 323–338, 14th Deep Sea Offshore Wind R&D Conference, EERA DeepWind 2017.
- [12] F.J. Madsen, T.R.L. Nielsen, T. Kim, H. Bredmose, A. Pegalajar-Jurado, R.F. Mikkelsen, A.K. Lomholt, M. Borg, M. Mirzaei, P. Shin, Experimental analysis of the scaled DTU10MW TLP floating wind turbine with different control strategies, *Renew. Energy* 155 (2020) 330–346.
- [13] N. Mendoza, A. Robertson, A. Wright, J. Jonkman, L. Wang, R. Bergua, T. Ngo, T. Das, M. Odeh, K. Mohsin, F.F. Flavia, B. Child, G. Bangga, M. Fowler, A. Goupee, R. Kimball, E. Lenfest, A. Viselli, Verification and validation of model-scale turbine performance and control strategies for the IEA wind 15 MW reference wind turbine, *Energies* 15 (20) (2022).
- [14] S. Gueydon, R. Lindeboom, W. van Kampen, E.-J. de Ridder, Comparison of two wind turbine loading emulation techniques based on tests of a TLP-FOWT in combined wind, waves and current, in: *ASME 2018 1st International Offshore Wind Technical Conference of International Conference on Offshore Mechanics and Arctic Engineering*, 2018, V001T01A012.
- [15] M. Thys, C. Souza, T. Sauder, N. Fonseca, P.A. Berthelsen, E. Engebretsen, H. Haslum, Experimental investigation of the coupling between aero- and hydrodynamical loads on a 12 MW semi-submersible floating wind turbine, in: *Ocean Renewable Energy of International Conference on Offshore Mechanics and Arctic Engineering*, Volume 9, 2021, V009T09A030.
- [16] F. Vittori, J. Azcona, I. Eguinoa, O. Pires, A. Rodríguez, Á. Morató, C. Garrido, C. Desmond, Model tests of a 10 MW semi-submersible floating wind turbine under waves and wind using hybrid method to integrate the rotor thrust and moments, *Wind Energy Sci.* 7 (5) (2022) 2149–2161.
- [17] O. Pires, J. Azcona, F. Vittori, I. Bayati, S. Gueydon, A. Fontanella, Y. Liu, E.-J. de Ridder, M. Belloli, J.W. van Wingerden, Inclusion of rotor moments in scaled wave tank test of a floating wind turbine using SiL hybrid method, *J. Phys. Conf. Ser.* 1618 (3) (2020) 032048.
- [18] A. Fontanella, Y. Liu, J. Azcona, O. Pires, I. Bayati, S. Gueydon, E.-J. de Ridder, J.W. van Wingerden, M. Belloli, A hardware-in-the-loop wave-basin scale-model experiment for the validation of control strategies for floating offshore wind turbines, *J. Phys. Conf. Ser.* 1618 (3) (2020) 032038.
- [19] R. Bergua, A. Robertson, J. Jonkman, E. Branlard, A. Fontanella, M. Belloli, P. Schito, A. Zasso, G. Persico, A. Sanvito, E. Amet, C. Brun, G. Campaña-Alonso, R. Martín-San-Román, R. Cai, J. Cai, Q. Qian, W. Maoshi, A. Beardsell, G. Pirrung, N. Ramos-García, W. Shi, J. Fu, R. Corniglion, A. Lovera, J. Galván, T.A. Nygaard, C.R. dos Santos, P. Gilbert, P.-A. Joulin, F. Blondel, E. Frickel, P. Chen, Z. Hu, R. Boisard, K. Yilmazlar, A. Croce, V. Harnois, L. Zhang, Y. Li, A. Aristondo, I. Mendikoa Alonso, S. Mancini, K. Boorsma, F. Savenije, D. Marten, R. Soto-Valle, C.W. Schulz, S. Netzband, A. Bianchini, F. Papi, S. Cioni, P. Trubart, D. Alarcon, C. Molins, M. Cormier, K. Briker, T. Lutz, Q. Xiao, Z. Deng, F. Haudin, A. Goveas, OC6 project Phase III: validation of the aerodynamic loading on a wind turbine rotor undergoing large motion caused by a floating support structure, *Wind Energy Sci.* 8 (4) (2023) 465–485.
- [20] I. Bayati, A. Facchinetti, A. Fontanella, F. Taruffi, M. Belloli, Analysis of FOWT dynamics in 2-DOF hybrid HIL wind tunnel experiments, *Ocean Eng.* 195 (2020).
- [21] M. Belloli, I. Bayati, A. Facchinetti, A. Fontanella, H. Giberti, F. La Mura, F. Taruffi, A. Zasso, A hybrid methodology for wind tunnel testing of floating offshore wind turbines, *Ocean Eng.* 210 (2020).
- [22] E. Gaertner, J. Rinker, L. Sethuraman, F. Zahle, B. Anderson, G. Barter, N. Abbas, F. Meng, P. Bortolotti, W. Skrzypinski, G. Scott, R. Feil, H. Bredmose, K. Dykes, M. Shields, C. Allen, A. Viselli, Definition of the IEA 15-Megawatt Offshore Reference Wind Turbine, Tech. rep., National Renewable Energy Laboratory, 2020, Available at <https://www.nrel.gov/docs/fy20osti/75698.pdf>.
- [23] R. Guanche, M. Somoano, T. Battistella, A. Rodriguez, S. Fernandez, J. Sarmiento, A. Alvarez, D. Blanco, A. Facchinetti, A. Fontanella, S. Di Carlo, V. Arramounet, F. Castillo, C. Molins, P. Trubart, S. Muñoz, I. Romero, F.J. Comas, D. Sisí, S. Doole, Integrated FOWT test report, 2023.
- [24] S. Ambrosini, I. Bayati, A. Facchinetti, M. Belloli, Methodological and technical aspects of a two-degrees-of-freedom hardware-in-the-loop setup for wind tunnel tests of floating systems, *J. Dyn. Syst. Meas. Control* 142 (6) (2020) 061002.
- [25] H. Giberti, F. La Mura, G. Resmini, M. Parmeggiani, Fully mechatronic design of an HIL system for floating devices, *Robotics* 7 (3) (2018).
- [26] R. Duran, S. Hernandez, F. Vigara, M.Y. Mahfouz, COREWIND - ACTIVEFLOAT OpenFAST model 15 MW FOWT grand canary Island site, 2020.
- [27] C. Molins, P. Trubart, M.Y. Mahfouz, UPC - WINDCRETE OpenFAST model 15MW FOWT - grand canary Island, 2020.
- [28] W. Cummins, The Impulse Response Function and Ship Motion, Technical Report 1661, David Taylor Model Basin-DTNSRDC, 1962.
- [29] T. Perez, T. Fossen, A matlab toolbox for parametric identification of radiation-force models of ships and offshore structures, *Model. Identif. Control* 30 (1) (2009).
- [30] A.J. Coulling, A.J. Goupee, A.N. Robertson, J.M. Jonkman, Importance of second-order difference-frequency wave-diffraction forces in the validation of a FAST semi-submersible floating wind turbine model, in: *Ocean Renewable Energy of International Conference on Offshore Mechanics and Arctic Engineering*, Volume 8, 2013, V008T09A019.
- [31] I. Bayati, A. Facchinetti, A. Fontanella, M. Belloli, 6-DoF hydrodynamic modelling for wind tunnel hybrid/HIL tests of FOWT: The real-time challenge, in: *Ocean Renewable Energy of International Conference on Offshore Mechanics and Arctic Engineering*, Volume 10, 2018, V010T09A078.
- [32] A. Fontanella, G. Da Pra, M. Belloli, Integrated design and experimental validation of a fixed-pitch rotor for wind tunnel testing, *Energies* 16 (5) (2023).
- [33] N.J. Abbas, D.S. Zalkind, L. Pao, A. Wright, A reference open-source controller for fixed and floating offshore wind turbines, *Wind Energy Sci.* 7 (1) (2022) 53–73.
- [34] N.J. Abbas, D.S. Zalkind, R.M. Mudafort, G. Hylander, S. Mulders, D. Heff, P. Bortolotti, NREL/ROSCO: RAAW v1.3, 2022.
- [35] T.J. Larsen, T.D. Hanson, A method to avoid negative damped low frequent tower vibrations for a floating, pitch controlled wind turbine, *J. Phys. Conf. Ser.* 75 (1) (2007) 012073.
- [36] G.J. van der Veen, I.J. Couchman, R.O. Bowyer, Control of floating wind turbines, in: *2012 American Control Conference (ACC)*, 2012, pp. 3148–3153.
- [37] J. Jonkman, Influence of control on the pitch damping of a floating wind turbine.